

Efficient and stable perovskite mini-module via high-quality homogeneous perovskite crystallization and improved interconnect

Received: 6 March 2024

Accepted: 24 July 2024

Published online: 06 August 2024

 Check for updatesHaitao Zhou^{1,2}, Kai Cai^{1,2}, Shiqi Yu^{1,2}, Zhenhan Wang^{1,2}, Zhuang Xiong^{1,2}, Zema Chu^{1,2}, Xinbo Chu^{1,2}, Qi Jiang^{1,2} & Jingbi You^{1,2}✉

The efficiency and stability of perovskite module devices are mainly limited by the quality of scalable perovskite films and sub-cells' lateral contact. Here, firstly, we report constant low temperature substrate to regulate the growth of perovskite intermediate films to slow down the crystallization for obtaining high-quality homogeneous perovskite films in large scale size, which avoid the effect of the ambient temperature on the film quality. Secondly, a scribing step named P1.5 was added before the top function layers deposition, the diffusion barrier layer can be formed “naturally” at the interconnection interface without introducing any additional materials, which well alleviates the diffusion degradation process. As a result, our inverted perovskite devices exhibit a very small efficiency loss with area expansion comparable to other photovoltaic devices (for example, Cadmium Telluride), the perovskite module (aperture area 14.61 cm²) shows a certified quasi-steady-state power conversion efficiency of 22.73%, and the module maintaining over 90% of its initial efficiency after 1000 hours of continuous operation under illumination.

After 15 years of fast development, the efficiency of the small size of perovskite solar cells (PSCs) was already over than 26%¹, for exploring the potential application of PSCs, developing efficient large-area devices is emergent.

Significant progress has been achieved for the perovskite solar cell modules, while it is still falling behind the small-size device efficiencies, which mainly could be due to the imperfect quality and uniformity of the perovskite layer in large-scale areas. To address this issue, different strategies for controlling the crystallization process, especially by using the high boiling temperature additive or the solvent, could coordinate with the lead halide^{2–10}. For example, Yang et al.⁵ used the additive diphenyl sulfoxide (DPSO) to enhance the nucleation barrier and stabilize the wet precursor film, and delivered a certified steady-state efficiency of 16.63% with an active area of 20.77 cm²; Yoo et al.⁶ ensured the balance between fast nucleation and slow crystal growth in the precursor solution by adding *n*-cyclohexyl-2-pyrrolidone (CHP) solvent and 17.53% mini-module

certified steady-state efficiency (aperture area 30.98 cm²) was achieved; Bu et al.^{9,10} utilized the *N*-methylpyrrolidone (NMP) solvent to coordinate with lead iodide to form a stable adduct and further added MAI additives to regulate the formation of the intermediate phases, achieving a laboratory reverse efficiency of 20.5% (aperture area 22.4 cm²). Recently, by embedding lead chelation molecules at the perovskite/hole transport interface to reduce the amorphous region at the buried interface, a 21.1% certified steady-state efficiency of the module (aperture area 26.9 cm²) has been demonstrated¹¹. Despite this, there is still a lot of room for power conversion efficiency (PCE) improvement of perovskite modules, and the efficiency loss with area amplification is still greater than that of other types of photovoltaic devices².

Another critical issue is module stability, to construct high PCE perovskite modules, three-step scribing (P1, P2, and P3) is usually needed to connect multiple sub-cells in series, but this traditional scribing design results in lateral direct contact between the perovskite

¹Laboratory of Semiconductor Physics, Institute of Semiconductors, Chinese Academy of Sciences, Beijing, P. R. China. ²Center of Materials Science and Optoelectronics Engineering, University of Chinese Academy of Sciences, Beijing, P. R. China. ✉e-mail: jyou@semi.ac.cn

and the metal electrode (near P2)^{2,12}, resulting interdiffusion and instability^{13–16}. To avoid this issue, before metal electrode deposition, a diffusion barrier layer (DBL) has been introduced by additional coatings such as two-dimensional nanostructured graphitic carbon nitride¹⁷, atomic layer deposited tin oxide¹⁸ or in situ reaction-generated lead oxide¹⁹, which improved the stability of the modules. From the perspective of simplifying the manufacturing process of renewable energy technologies and improving module stability, developing simple solutions to construct effective DBLs is important to lower the barriers toward commercialization.

Herein, firstly, we show a simple low-temperature substrate growth (LTSG) solution to deposit high-quality homogeneous crystallinity large-area perovskite, and more importantly, the process is inert with the ambient temperature (environment temperature during spin-coating/vacuum chamber/annealing) variation. As a result, the absolute value of PCE decreases by only about 0.75% for each order of magnitude increase in the device area of our inverted structural devices. Secondly, we designed a simple one-step P1.5 scribing and “naturally” introduced an effective DBL without additional deposition. According

to these two strategies, a certified quasi-steady-state PCE of 22.73% was obtained for the inverted structure PSCs mini-module (aperture area 14.61 cm²). In addition, after 1000 h of operation at the maximum power point (MPP), the module can retain over 90% of its initial PCE.

Results

Homogeneous perovskite films deposition for large area

We chose FA_{0.93}MA_{0.02}CS_{0.05}PbI_{2.94}Br_{0.06} as absorbing layer^{20–22}. The schematic diagram of the fabrication process of our perovskite films is shown in Fig. 1a, and the detailed experimental process is included in the experimental section. Firstly, we obtained a flat precursor wet film by spin coating or slot-die coating. Note that the spin coating here is set up as a short-time (e.g., 3 s) process, and the same as the slot-die coating with a precursor wet film with almost no solvent volatilization, aiming to approximate the reality of future industrial coatings. We then use the vacuum extraction method^{23–25} to remove the solvent and obtain the intermediate film. Generally, perovskite nucleation growth can affect the quality of the intermediate film, which in turn affects the quality of the annealed perovskite film^{5,6,8–10,12,26}. Here, to slow down the

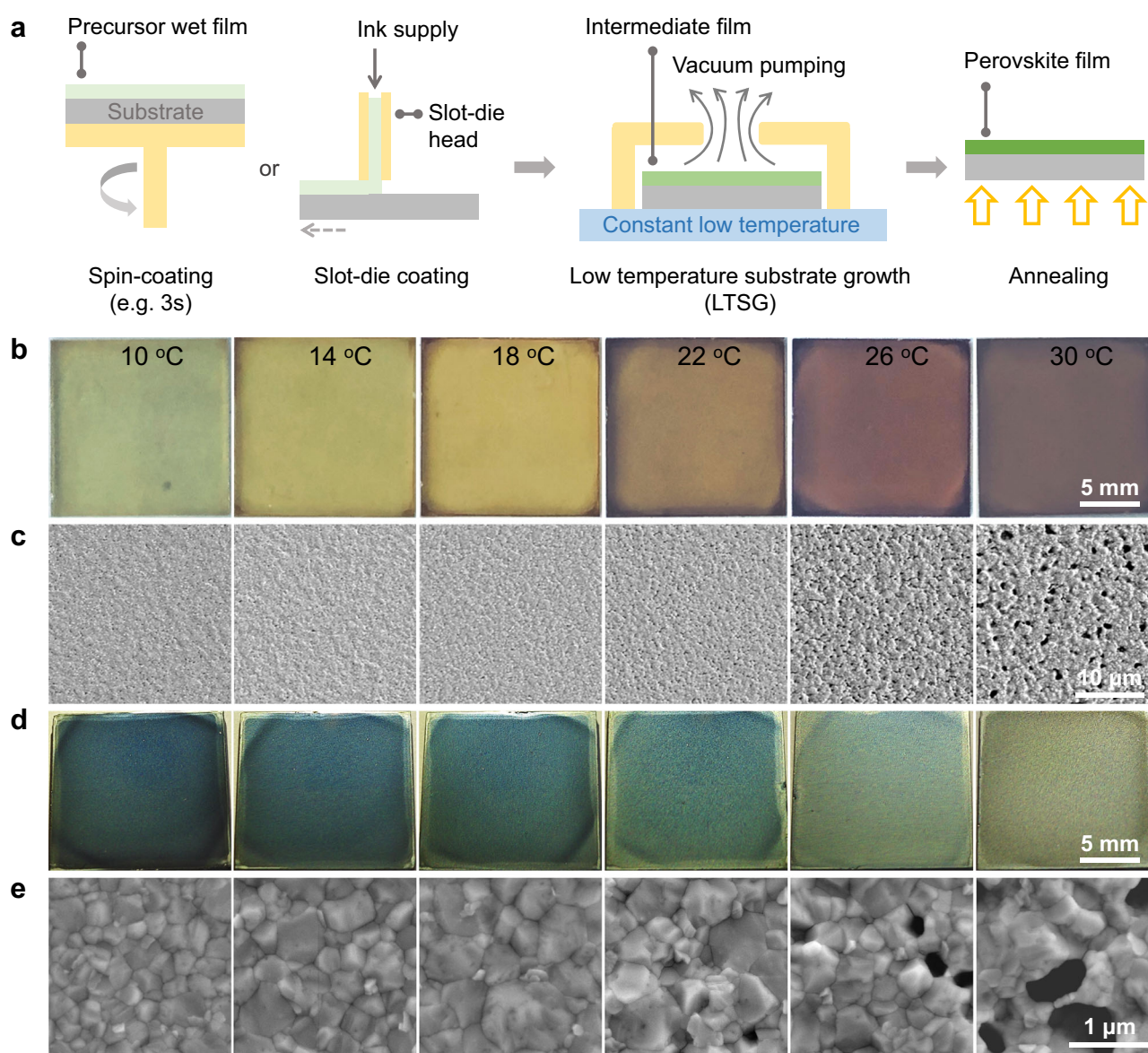


Fig. 1 | Films fabrication and morphology characterizations. **a** Schematic diagram of the fabrication process of perovskite films using low-temperature substrate growth (LTSG). e.g., exempli gratia. Optical photos **(b)** and **(d)** and SEM

images **(c)** and **(e)** of the intermediate films and perovskite films corresponding to different LTSG temperatures.

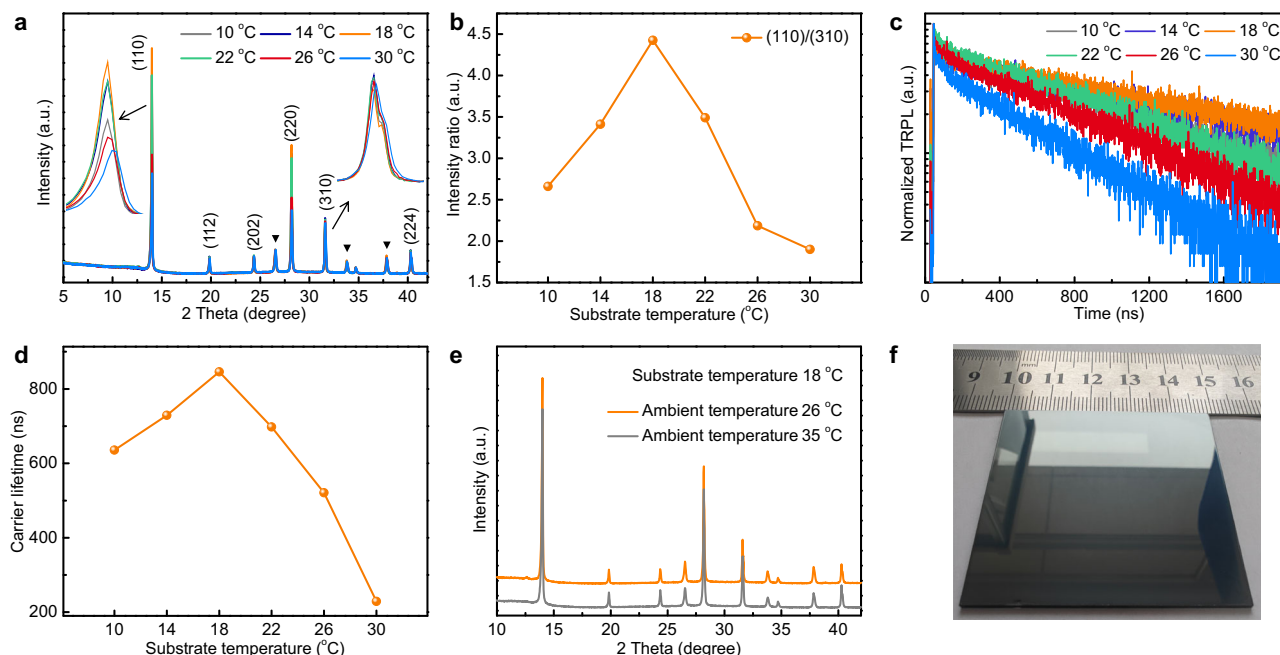


Fig. 2 | Characterization of perovskite films fabricated by LTSG. XRD (a) and (b) and TRPL (c) and (d) results of perovskite films obtained at different LTSG temperatures (10 to 30 °C). The peaks corresponding to the black inverted triangle are

from the FTO substrate. **e** XRD of perovskite films fabricated at 26 °C and 35 °C ambient temperature, while the LTSG temperatures were both 18 °C. a.u., arbitrary units. **f** The optical photo of the 5 cm × 5 cm large area perovskite film.

growth of the intermediate film for obtaining homogeneous film in large scale size, we regulate its growth using low temperature substrate growth (LTSG, Fig. 1a) process by simply lowering the substrate temperature.

We found that the color of the intermediate film gradually became darker as the LTSG temperature increased from 10 to 30 °C (ambient temperature about 26 °C) (Fig. 1b), and the optical absorption intensity became stronger (Supplementary Fig. 1), indicating there is a phase transition under higher LTSG temperature. It is easy to understand that the higher temperature not only enhances the solvent extraction but, more importantly, provides energy for the nucleation and growth of perovskite.

We checked the morphologies of the intermediate films before annealing, we found that the films were dense when the LTSG temperatures were below 18 °C, while large pinholes were formed over 18 °C (Fig. 1c). These could be explained that the intermediate films growth is partially frozen at low temperature, while higher temperature could result in unwanted faster nucleation and growth.

We also checked the morphologies of the perovskites obtained after annealing the above intermediate films. From the microscopy images (Fig. 1d), it can be found that as the LTSG temperature decreases, the film surface becomes darker and brighter, under higher LTSG temperature, the perovskite film become gray. Consistent with the intermediate film states, we found that the perovskite films showed dense and high crystallinity while processed at LTSG temperatures not exceeding 18 °C, while at higher temperatures, even though the crystal size is larger, the films exhibit more pinholes (Fig. 1e). The cross-sectional SEM results confirmed that the LTSG strategies can deliver uniform, non-porous and large crystal size at moderate LTSG temperature (Supplementary Fig. 2).

We have also carried out the X-ray diffraction to check the crystallinity of the perovskite films, it can be found that the perovskite films we obtained are all black phases (Fig. 2a). It is very interesting that the (110)/(310) peak intensity ratio for the perovskite film processed at LTSG-18 °C is the highest (Fig. 2b), indicating that preferred orientation processed at LTSG-18 °C. It is reported that the preferred

orientation of the diffraction peak near 14 ° is beneficial to increasing carrier mobility and reducing defect density^{27–29}. Photoluminescence (PL) results (Supplementary Fig. 3) show that the perovskite film fabricated with an LTSG-18 °C has the strongest PL peak, indicating that the film has the lowest defect state density. In addition, it was also found that as the LTSG temperature increased to 30 °C, the PL peak position red-shifted from 797 nm to 809 nm, which was speculated to be related to defects. The time-resolved photoluminescence (TRPL) results (Fig. 2c, d) show that the perovskite film fabricated at an LTSG-18 °C has the longest carrier lifetime (846 ns), which decreases to 636 and 229 ns as the LTSG temperature decreases to 10 °C and increases to 30 °C, respectively. This further indicates the improvement of the crystal quality of the perovskite film while the nucleation growth of the intermediate film is delayed at moderate LTSG temperature.

We also investigated whether the LTSG is affected by ambient temperature. When we prepared the intermediate films at different ambient temperatures, such as under the ambient temperature of 26 °C or a higher temperature of 35 °C, we found almost no difference in the XRD diffraction peaks (Fig. 2e), SEM morphologies (Supplementary Fig. 4), and device performance (Supplementary Fig. 5, see below for device structures), indicating that the LTSG is insensitive to the surrounding environment.

Based on the LTSG technique, we fabricated large-area perovskite films on a 5 cm × 5 cm FTO substrate, it can be clearly seen that the perovskite film is pretty uniform and mirror-like (Fig. 2f). In order to check the uniformity of the obtained perovskite film, we divided the substrate into 9 parts, and the tested steady-state PL, TRPL, absorption, and XRD patterns were almost overlapping or similar in these 9 regions (Supplementary Fig. 6). SEM morphology in different areas and at different scales also show uniform and similar morphologies (Supplementary Fig. 7). These results confirmed that the large-area perovskite film formed by this LTSG is homogeneous.

After obtaining a high-quality perovskite layer, we first constructed small size (0.102 cm²) device with the structure of FTO/NiO_x/Me-4PACz/perovskite/PEACI/PCBM/SnO₂/Cu (Supplementary Fig. 8). The device based on the perovskite film fabricated under LTSG-18 °C

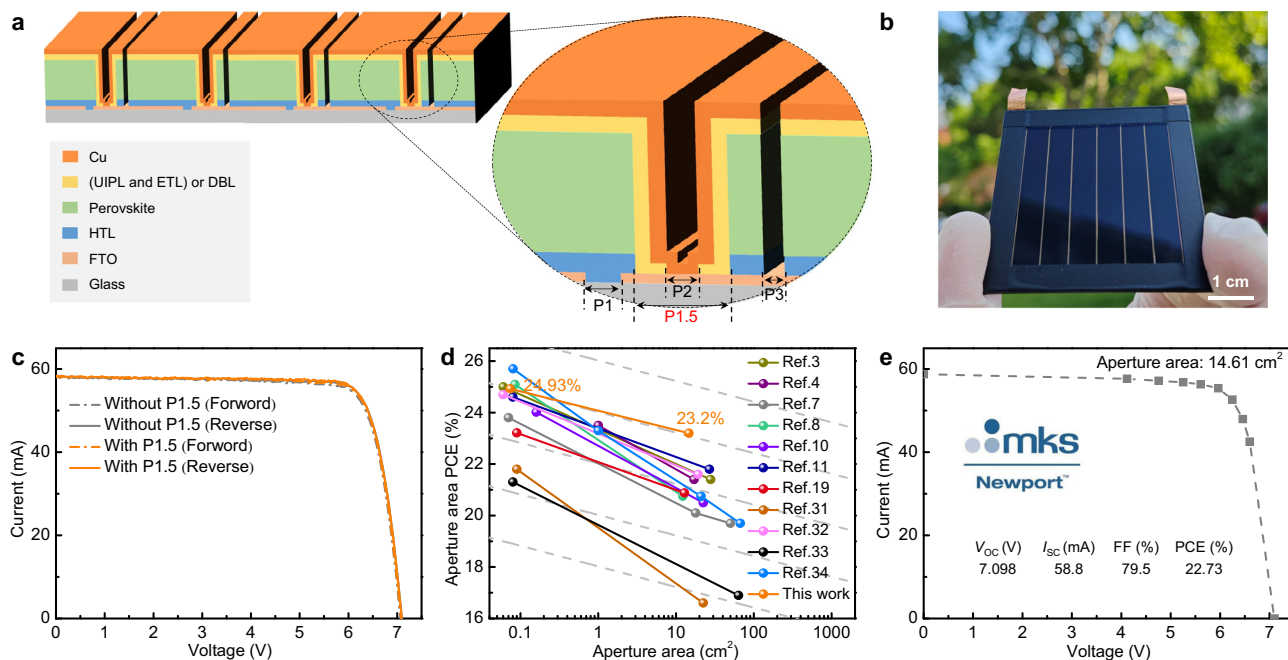


Fig. 3 | Construction of diffusion barrier layers (DBLs) by P1.5, and modules performance. **a** Schematic diagram of the structure of a module with a DBL built at the interconnection interface by P1.5. UIPL is the upper interface passivation layer. **b** Image of a module. **c** Forward and reverse scan I - V curves of modules with and without P1.5 (DBL). **d** Comparison of the device PCE from small size to large size.

The dotted line represents a 0.8% decrease in the absolute value of PCE for each order of magnitude increase in area. **e** Certified quasi-steady-state I - V measurement conducted at Newport, including the performance parameters. The certified aperture area of this module is 14.61 cm^2 .

condition showing the best device efficiency, we obtained 24.93% under reverse scans with the open circuit voltage of 1.187 V, short circuit current density of 25.39 mA/cm^2 and fill factor of 82.75% (Supplementary Fig. 9).

P1.5 “naturally” builds DBL and module performance

In the traditional perovskite module fabrication process, P2 cutting should be carried out after depositing all the functional layers, and then the metal electrode was deposited to connect each sub-cell in series^{2,12,30}. This process leads to an unavoidable halide-metal electrode contact interface where diffusion reactions occur, which limits the stability of the module¹⁷⁻¹⁹. We add an additional cutting process after perovskite layer growth, named P1.5 (Fig. 3a and Supplementary Figs. 10, 11, 12). After P1.5, function layers of PEACl and PCBM/SnO₂ were deposited, and then P2 was carried out, since the width of P1.5 is slightly wider than that of the P2, the top function layer will still remain and the diffusion barrier layer “naturally” formed (Supplementary Fig. 13). Compared with the reported halide-metal electrode interface modification solutions with the introduction of additional materials¹⁷⁻¹⁹, the advantages proposed in this study is that one additional step of simple scribing process is required, and P1.5 has no negative effect on the efficiency, which will be shown later.

Based on the above-mentioned LTSG and P1.5 strategies, we fabricated a perovskite solar module (aperture area 14.625 cm^2) with 6 sub-cells on a 5 $cm \times 5$ cm substrate (Fig. 3b). Typically, the laser scribing process is performed in ambient air. We found that the devices with and without P1.5 show similar efficiency and low hysteresis (Fig. 3c and Supplementary Table 1), indicating there is no significant degradation even though patterning the perovskite layer with high energy laser. The performance statistics of the 22 perovskite modules we fabricated are shown in Supplementary Fig. 14, inferring that the device showed good reproducibility, with an average PCE of 22.79% for these modules, the best PCE is 23.2%. Considering the geometry fill factor (GFF) of 94.7% (Supplementary Fig. 15), the active

area PCE of our best module is 24.5%, which is close to the performance of our small-size devices.

It is reported that the absolute value of PCE of different types of photovoltaic devices (such as silicon and CdTe) decreases by about 0.8% with every order of magnitude increase in device area². We calculate that the absolute value of PCE of our device decreases by 0.75% for every order of magnitude increase in aperture area (The aperture area increases from 0.0737 to 14.625 cm^2 , the efficiency loss is 1.73%), which is comparable to the efficiency loss of other types of photovoltaic cells, and is better than other reported perovskite cell module works (Fig. 3d and Supplementary Table 2)^{3,4,7,8,10,11,19,31-34}. By comparing the performance parameters of our champion PCE small-area and large-area devices (Supplementary Table 3), we noticed that the main loss comes from the loss of short circuit current density. Therefore, increasing the geometric fill factor in the future is an important way to further reduce efficiency losses. We sent the best module to an accredited laboratory (Newport, USA) for certification. This module provided a certified quasi-steady-state PCE of 22.73% (Fig. 3e and Supplementary Fig. 16), which is the highest certified steady-state PCEs of perovskite solar modules with aperture areas > 10 cm^2 among all reported works (Supplementary Fig. 17 and Supplementary Table 4)^{6,7,11,19,31-33,35,36}.

We also tested the LTSG and P1.5 strategies when do slot-die coated perovskite films with the same device structure, a PCE of 22.96% was achieved with an aperture area of 14.625 cm^2 (Supplementary Fig. 18), indicating the universal and general usage of the strategies for future applications towards commercialization.

P1.5 (DBL) improves module stability

We investigated the stability of unencapsulated modules aging in air (25 °C temperature and 30–40% humidity). After aging for 328 h (Fig. 4a and Supplementary Fig. 19), we found that the module without P1.5 decreased to 60% of the initial PCE, with the FF, I_{SC} , and V_{OC} loss are 29.6%, 9.9%, and 5.2%, respectively, the module with P1.5 still

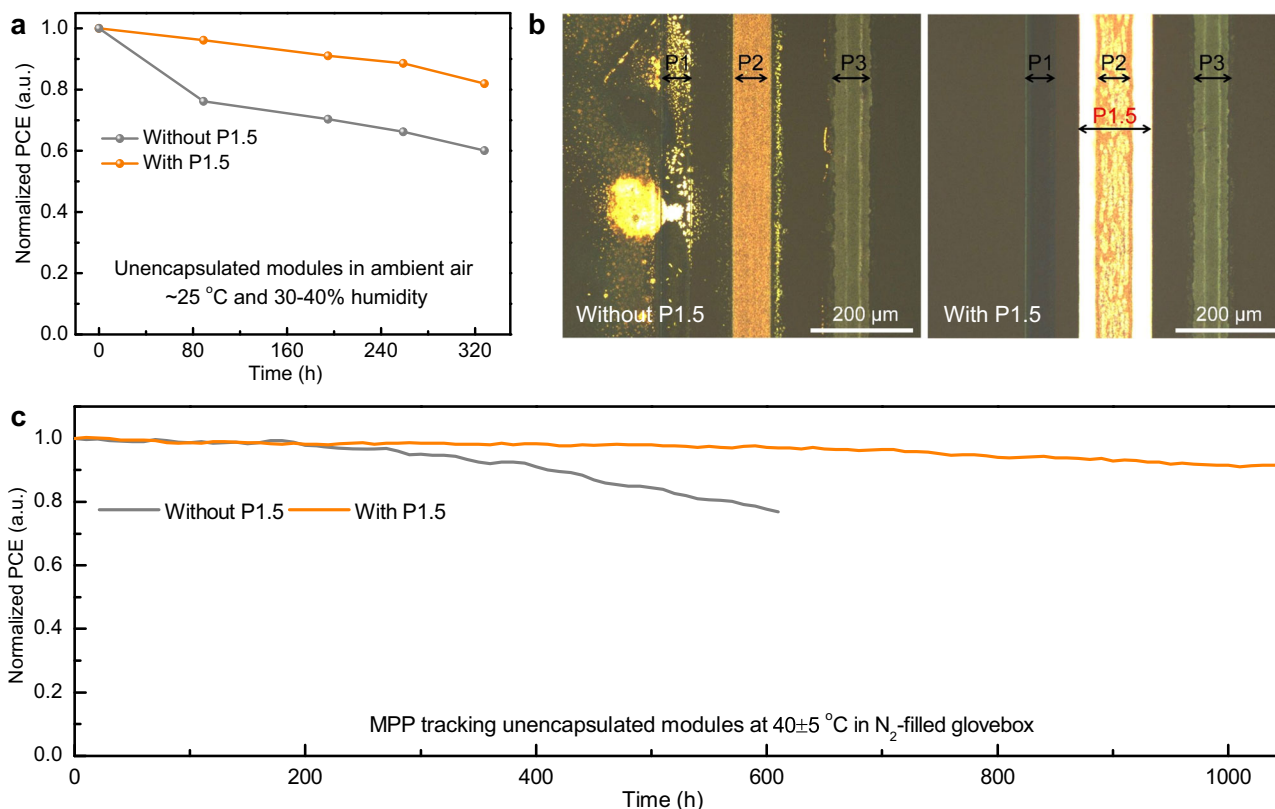


Fig. 4 | Stability of unencapsulated modules. **a** Aging stability tracking of modules in ambient air (25 °C, 30–40% humidity). **b** Optical micrograph of the interconnect region of the modules after aging for 328 h in ambient air. **c** Long-term MPP operational stability results of modules under simulated 1-sun illumination in a N₂ glove box.

maintains 82% of the initial PCE, with FF, I_{SC} , and V_{OC} loss are 12.2%, 4.9%, and 1.9%, respectively. Optical microscopy testing was performed on the interconnect region after aging (Fig. 4b), and it was found that the module without P1.5 showed significant corrosion degradation near P2 and in the active area of the adjacent sub-cell (P1 side). While for the module with P1.5, no significant degradation was observed. It is also worth noting that there is no significant degradation in the vicinity of the P3 side away from P2 in both devices (Fig. 4b). This suggests that this corrosion degradation is related to the direct contact between the metal and the perovskite, and not just caused by water and oxygen in the air. DBL constructed by P1.5 suppressed the diffusion and avoided the metal-halide reaction. We have carried out light beam-induced current (LBIC) measurements for the device with and without P1.5, we found that after air aging, the P1.5 device has a more uniform, bright, and clear response image compared to the non P1.5 device (Supplementary Fig. 20), further demonstrating the anti-degradation effect of P1.5 (DBLs).

We further performed accelerated aging tests at 85 °C (nitrogen (N₂) atmosphere) for unencapsulated perovskite modules. The module without P1.5 decays to 46.8% of the initial PCE after aging for 442 h, while the modules with P1.5 still maintain 66.7% of the initial PCE (Supplementary Fig. 21). In order to observe the diffusion behavior more intuitively, we use an SEM with energy dispersive X-rays for elemental analysis (Supplementary Fig. 22). After 100 h of thermal aging, the I-Cu interdiffusion in the perovskite/Cu sample occurred at the direct perovskite/electrode contact and extended to the entire perovskite/metal layer. While the halide-metal interdiffusion is largely hindered by the DBLs.

Benefiting from the well-inhibited diffusion degradation process, it is very encouraging that the maximum power point tracking (MPPT) stability of our module is greatly improved (Fig. 4c). The module with P1.5 maintains over 90% of its initial PCE after 1050 h of continuous

operation under simulated one solar illumination (N₂, about 40 °C) with the initial efficiency of 22.4% (when tested under room temperature), while module without P1.5 only maintains below 80% of its initial PCE after 610 h of operation (Fig. 4c). We noticed that the loss of PCE of P1.5 module after MPPT mainly comes from the decrease of open circuit voltage (Supplementary Fig. 23), which could be due to the passivation layer degraded.

In summary, we have developed a low temperature substrate method to regulate the growth of perovskite intermediate films for obtaining high-quality homogeneous perovskite films, this simple strategy addressed the difficulty in controlling ambient temperature. For enhancing the mini-module device stability, a P1.5 method has been invented for forming a “natural” buffer layer to suppress the diffusion degradation process. As a result, the perovskite module (aperture area 14.61 cm²) shows a certified quasi-steady-state power conversion efficiency of 22.73%, which is the highest efficiency up to now for similar sizes of devices. The module maintains good stability under continuous operation under illumination. The approaches found in this study will push forward the perovskite large-size device for practical applications.

Methods

Materials

NiO_x nanoparticle powders (particle size around 10 nm), lead iodide (PbI₂), formamidinium iodide (FAI), methylammonium chloride (MACl), phenethylammonium chloride (PEACl), cesium iodide (CsI), lead bromide (PbBr₂), methylammonium bromide (MABr), PCBM were purchased from Advanced Election Technology Company in China. N-methylpyrrolidone (NMP), dimethylformamide (DMF), chlorobenzene (CB), and isopropanol (IPA) were purchased from Sigma Aldrich. All the chemicals are used directly without further purification.

Perovskite film fabrication

The $\text{FA}_{0.93}\text{MA}_{0.02}\text{Cs}_{0.05}\text{PbI}_{2.94}\text{Br}_{0.06}$ (15% MAcl and 5% excess PbI_2) precursor in DMF:NMP (6:1 volume ratio) was deposited on the FTO/HTL substrate (small area $1.5\text{ cm} \times 1.5\text{ cm}$, large area $5\text{ cm} \times 5\text{ cm}$) by spin coating or slot-die printing. The 1.6 M precursor solution was deposited on the FTO/HTL substrate at 4000 rpm for a short time of 3 s under a spin-coating process. Under the slot-die printing process, the precursor solution concentration is 1.3 M, the distance between the FTO/HTL substrate and the slot-die lip is 0.25 mm, the printing speed is 5 mm/s, and the liquid supply rate is 0.1 ml/min. Then all the obtained perovskite precursor wet film was moved to a vacuum chamber and pumped at about 20 Pa for 60 s. In a vacuum process, the growth of the intermediate films is regulated under a low substrate temperature (e.g., 18 °C). It is then annealed at 110 °C for 15 min to obtain a perovskite film.

Perovskite solar cell fabrication

Glass/FTO substrate was ultrasonically cleaned sequentially with detergent, deionized water, acetone, and IPA. The substrate was cleaned with UV-ozone for 10 min before use. A 15 mg/ml NiO_x aqueous solution with added H_2O_2 (40 mol% of NiO_x) was spin-coated on the substrate at 1500 rpm for 30 s and annealed at 150 °C in ambient air for 10 min. Spin-coat 0.5 mg/ml Me-4PACz IPA solution on NiO_x at 4000 rpm for 30 s and anneal at 100 °C for 10 min. Perovskite films were deposited on the substrate as detailed above. 1 mg/ml PEACl IPA solution was deposited on the perovskite at 4000 rpm for 30 s and annealed at 100 °C for 10 min, and then 20 mg/ml PCBM CB solution was spin-coated at 2000 rpm for 30 s. The substrate was then transferred to the atomic layer deposition (ALD) system for SnO_2 layer deposition, the deposition parameter can be found in elsewhere³⁷. Finally, Cu film as an electrode was deposited by thermal evaporation.

Large area mini-module fabrication

Compared with the fabrication of each functional layer of a small-area solar cell, except for the corresponding increase in the amount of solution, other parameters remain unchanged. A perovskite module with 6 series sub-cells was fabricated on a glass/FTO substrate with a size of $5\text{ cm} \times 5\text{ cm}$. The series interconnection of modules was realized through P1, P1.5, P2, and P3 lines (Fig. 3a and Supplementary Fig. 10). The role of P1.5 is to create a horizontal diffusion barrier layer (DBL) in a simple, efficient, and natural way. Pattern the lines using a laser scribing system with a wavelength of 532 nm, a frequency of 100 KHz, a power of 7.2 W, and a pulse width of 16.3 ns. P1, P1.5, P2, and P3 are scribed before cleaning the FTO substrate, after perovskite deposition, and before and after evaporation electrodes. The widths of P1, P1.5, P2, P3, and dead area are 50, 141, 73, 68 and 395 μm , respectively. The geometric fill factor (GFF) is 94.7%.

Characterizations

The XRD patterns of the films were obtained on a D8 ADVANCE system (Bruker Nano Inc.) using $\text{Cu K}\alpha$ radiation ($\lambda = 1.5405\text{ \AA}$) as the X-ray source. The ultraviolet-visible absorption spectra were acquired using a Cary 5000 spectrometer. Steady-state PL and time-resolved PL (TRPL) spectra were measured by an FLS1000 spectrometer. The scanning electron microscopy (SEM) images were acquired using a field-emission scanning electron microscopy (FEI NanoSEM650), which uses an electron beam accelerated at 0.5 to 30 kV, enabling operation at a variety of currents. The J - V characteristics of the devices were obtained using a Keithley 2400 Source Meter under simulated one-sun AM 1.5 G illumination (100 mW/cm^2) with a solar simulator (Enlitech, SS-F5-3A), and the light intensity was calibrated by means of a KG-5 Si diode. The aperture areas of metal masks for small-area and large-area devices are 0.0737 and 14.625 cm^2 , respectively. The devices were measured both in reverse scan (1.2 V to 0 V, step 0.02 V or 7.2 V to 0 V, step 0.02 V) and forward scan (0 V to 1.2 V, step 0.02 V or 0 V to

7.2 V, step 0.02 V). The EQE was measured using an Enlitech EQE measurement system (QE-R3018). We sent the best module to an accredited laboratory (Newport, USA) for certification. The MPP operation stability test of the module under continuous white LED illumination was carried out in a nitrogen glove box. Module thermal stability aging experiments were performed on a hot plate at 85 °C in a nitrogen glove box. Module ambient air aging experiments were performed in ambient air at 25 °C and 30–40% humidity.

Reporting summary

Further information on research design is available in the Nature Portfolio Reporting Summary linked to this article.

Data availability

All data generated or analyzed during this study are included in the published article and its Supplementary Information. Additional data are available from the corresponding author upon request.

References

1. National Renewable Energy Laboratory, Photovoltaic Research: Best Research-Cell Efficiency Chart. <https://www.nrel.gov/pv/cell-efficiency.html> (2024).
2. Li, Z. et al. Scalable fabrication of perovskite solar cells. *Nat. Rev. Mater.* **3**, 18017 (2018).
3. Shi, P. et al. Oriented nucleation in formamidinium perovskite for photovoltaics. *Nature* **620**, 323–327 (2023).
4. You, S. et al. Radical polymeric p-doping and grain modulation for stable, efficient perovskite solar modules. *Science* **379**, 288–294 (2023).
5. Yang, Z. et al. Slot-die coating large-area formamidinium-cesium perovskite film for efficient and stable parallel solar module. *Sci. Adv.* **7**, eabg3749 (2021).
6. Yoo, J. W. et al. Efficient perovskite solar mini-modules fabricated via bar-coating using 2-methoxyethanol-based formamidinium lead tri-iodide precursor solution. *Joule* **5**, 2420–2436 (2021).
7. Chen, S. et al. Stabilizing perovskite-substrate interfaces for high-performance perovskite modules. *Science* **373**, 902–907 (2021).
8. Miao, Y. et al. Green solvent enabled scalable processing of perovskite solar cells with high efficiency. *Nat. Sustain.* **6**, 1465–1473 (2023).
9. Bu, T. et al. Lead halide-templated crystallization of methylamine-free perovskite for efficient photovoltaic modules. *Science* **372**, 1327–1332 (2021).
10. Bu, T. et al. Modulating crystal growth of formamidinium-cesium perovskites for over 200 cm^2 photovoltaic sub-modules. *Nat. Energy* **7**, 528–536 (2022).
11. Fei, C. et al. Lead-chelating hole-transport layers for efficient and stable perovskite minimodules. *Science* **380**, 823–829 (2023).
12. Park, N.-G. & Zhu, K. Scalable fabrication and coating methods for perovskite solar cells and solar modules. *Nat. Rev. Mater.* **5**, 333–350 (2020).
13. Bi, E. et al. Diffusion engineering of ions and charge carriers for stable efficient perovskite solar cells. *Nat. Commun.* **8**, 15330 (2017).
14. Lin, X. et al. In situ growth of graphene on both sides of a cu-ni alloy electrode for perovskite solar cells with improved stability. *Nat. Energy* **7**, 520–527 (2022).
15. Boyd, C. C. et al. Barrier design to prevent metal-induced degradation and improve thermal stability in perovskite solar cells. *ACS Energy Lett.* **3**, 1772–1778 (2018).
16. Li, J., Dong, Q., Li, N. & Wang, L. Direct evidence of ion diffusion for the silver-electrode-induced thermal degradation of inverted perovskite solar cells. *Adv. Energy Mater.* **7**, 1602922 (2017).
17. Bi, E. et al. Efficient perovskite solar cell modules with high stability enabled by iodide diffusion barriers. *Joule* **3**, 2748–2760 (2019).

18. Xiao, K. et al. Scalable processing for realizing 21.7%-efficient all-perovskite tandem solar modules. *Science* **376**, 762–767 (2022).
19. Gao, Y. et al. Efficient and stable perovskite solar modules enabled by inhibited escape of volatile species. *Adv. Mater.* **36**, 2309310 (2024).
20. Li, C. et al. Rational design of lewis base molecules for stable and efficient inverted perovskite solar cells. *Science* **379**, 690–694 (2023).
21. Li, Z. et al. Organometallic-functionalized interfaces for highly efficient inverted perovskite solar cells. *Science* **376**, 416–420 (2022).
22. Jiang, Q. et al. Towards linking lab and field lifetimes of perovskite solar cells. *Nature* **623**, 313–318 (2023).
23. Li, X. et al. A vacuum flash-assisted solution process for high-efficiency large-area perovskite solar cells. *Science* **353**, 58–62 (2016).
24. Du, M. et al. Surface redox engineering of vacuum-deposited NiO_x for top-performance perovskite solar cells and modules. *Joule* **6**, 1931–1943 (2022).
25. Ding, Y. et al. Single-crystalline TiO₂ nanoparticles for stable and efficient perovskite modules. *Nat. Nanotechnol.* **17**, 598–605 (2022).
26. Li, F. et al. Hydrogen-bond-bridged intermediate for perovskite solar cells with enhanced efficiency and stability. *Nat. Photonics* **17**, 478–484 (2023).
27. Zheng, X. et al. Managing grains and interfaces via ligand anchoring enables 22.3%-efficiency inverted perovskite solar cells. *Nat. Energy* **5**, 131–140 (2020).
28. Ma, C. et al. Photovoltaically top-performing perovskite crystal facets. *Joule* **6**, 2626–2643 (2022).
29. Luo, C. et al. Facet orientation tailoring via 2D-seed-induced growth enables highly efficient and stable perovskite solar cells. *Joule* **6**, 240–257 (2022).
30. Jiang, D. et al. Non-laser and all-vapor-phase processed perovskite solar modules stabilized by naturally formed barrier layers. *Joule* **8**, 1161–1175 (2024).
31. Liu, Z. et al. A holistic approach to interface stabilization for efficient perovskite solar modules with over 2,000-hour operational stability. *Nat. Energy* **5**, 596–604 (2020).
32. Huang, Y. et al. Finite perovskite hierarchical structures via ligand confinement leading to efficient inverted perovskite solar cells. *Energy Environ. Sci.* **16**, 557–564 (2023).
33. Deng, Y. et al. Tailoring solvent coordination for high-speed, room-temperature blading of perovskite photovoltaic films. *Sci. Adv.* **5**, eaax7537 (2019).
34. Kim, M. et al. Conformal quantum dot-SnO₂ layers as electron transporters for efficient perovskite solar cells. *Science* **375**, 302–306 (2022).
35. Gao, Y. et al. Can nanosecond laser achieve high-performance perovskite solar modules with aperture area efficiency over 21%? *Adv. Energy Mater.* **12**, 2202287 (2022).
36. Deng, Y. et al. Defect compensation in formamidinium-caesium perovskites for highly efficient solar mini-modules with improved photostability. *Nat. Energy* **6**, 633–641 (2021).
37. Xiao, K. et al. All-perovskite tandem solar cells with 24.2% certified efficiency and area over 1 cm² using surface-anchoring zwitterionic antioxidant. *Nat. Energy* **5**, 870–880 (2020).

Acknowledgements

This work was supported by the National Natural Science Foundation of China (Grant Numbers: 61925405, J. Y.), the National Key Research and Development Program of China (Grant Number. 2020YFB1506400, J. Y.), and CAS Project for Young Scientists in Basic Research (grant YSBR-090, J. Y.).

Author contributions

J. Y., H. Z. conceived the idea, H. Z. fabricated and characterized the devices, K. C. take part in device fabrication and preparation device, S. Y., Z. W., Z. X., Z. C., X. C., and Q. J. were involved in data analysis. J. Y. directed and supervised the project. J. Y. and H. Z. co-wrote the manuscript. All authors contributed to discussions and finalizing the manuscript. There are no competing financial interests.

Competing interests

The authors declare no competing interests.

Additional information

Supplementary information The online version contains supplementary material available at <https://doi.org/10.1038/s41467-024-50962-1>.

Correspondence and requests for materials should be addressed to Jingbi You.

Peer review information *Nature Communications* thanks Yaohua Mai and the other anonymous, reviewer(s) for their contribution to the peer review of this work. A peer review file is available.

Reprints and permissions information is available at <http://www.nature.com/reprints>

Publisher's note Springer Nature remains neutral with regard to jurisdictional claims in published maps and institutional affiliations.

Open Access This article is licensed under a Creative Commons Attribution-NonCommercial-NoDerivatives 4.0 International License, which permits any non-commercial use, sharing, distribution and reproduction in any medium or format, as long as you give appropriate credit to the original author(s) and the source, provide a link to the Creative Commons licence, and indicate if you modified the licensed material. You do not have permission under this licence to share adapted material derived from this article or parts of it. The images or other third party material in this article are included in the article's Creative Commons licence, unless indicated otherwise in a credit line to the material. If material is not included in the article's Creative Commons licence and your intended use is not permitted by statutory regulation or exceeds the permitted use, you will need to obtain permission directly from the copyright holder. To view a copy of this licence, visit <http://creativecommons.org/licenses/by-nc-nd/4.0/>.

© The Author(s) 2024